View metadata, citation and similar papers at core.ac.uk

brought to you by CORE

provided by Biblioteca Digital da Produção Intelectual da Universidade de São Paulo (BDPI/USP)

Universidade de São Paulo

Biblioteca Digital da Produção Intelectual - BDPI

Departamento de Física e Ciências Materiais - IFSC/FCM

Artigos e Materiais de Revistas Científicas - IFSC/FCM

2009-01

Microstructure, dielectric properties and optical band gap control on the photoluminescence behavior of Ba['Zr IND.0.25''Ti IND. 0.75]'O IND.3' thin films

Journal of Sol-Gel Science and Technology,Dordrecht,v. 49, n. 1, p. 35-46, Jan. 2009
http://www.producao.usp.br/handle/BDPI/49354

Downloaded from: Biblioteca Digital da Produção Intelectual - BDPI, Universidade de São Paulo

J Sol-Gel Sci Technol (2009) 49:35–46
DOI 10.1007/s10971-008-1841-x

ORIGINAL PAPER

Microstructure, dielectric properties and optical band gap control on the photoluminescence behavior of $Ba[Zr_{0.25}Ti_{0.75}]O_3$ thin films

L. S. Cavalcante · J. C. Sczancoski · F. S. De Vicente · M. T. Frabbro · M. Siu Li · J. A. Varela · E. Longo

Received: 14 March 2008 / Accepted: 2 October 2008 / Published online: 24 October 2008
© Springer Science+Business Media, LLC 2008

Abstract $Ba[Zr_{0.25}Ti_{0.75}]O_3$ (BZT) thin films were synthesized by the complex polymerization method and heat treated at 400 °C for different times and at 700 °C for 2 h. These thin films were analyzed by X-ray diffraction (XRD), Fourier-transform infrared (FT-IR) spectroscopy, field emission gun-scanning electron microscopy (FEG-SEM) and atomic force microscopy (AFM), Ultraviolet–visible (UV–vis) absorption spectroscopy, electrical and photoluminescence (PL) measurements. FEG-SEM and AFM micrographs showed that the microstructure and thickness of BZT thin films can be influenced by the processing times. Dielectric constant and dielectric loss of BZT thin films heat treated at 700 °C were approximately 148 and 0.08 at 1 MHz, respectively. UV–vis absorption spectra suggested the presence of intermediary energy levels (shallow and deep holes) within the band gap of BZT thin films. PL behavior was explained through the optical band gap values associated to the visible light emission components.

Keywords Microstructure · Dielectric · Optical band gap · Photoluminescence · BZT thin films

1 Introduction

Recently, barium zirconate titanate, $Ba[Zr,Ti]O_3$ (BZT), has been utilized as an alternative material to barium strontium titanate, $[Ba,Sr]TiO_3$, in the preparation of thin films or ceramic bulks [1–3]. This material presents a perovskite-type structure with general formula ABO_3 (A = Ba and B = Ti, Zr). Generally, BZT are formed by solid solution between barium titanate (BTO) and barium zirconate (BZO) due to the substitution of Ti^{4+} ions (B site) (atomic weight of 47.9, ionic radius of 74.5 pm) by Zr^{4+} ions (atomic weight of 91.2, atomic radius of 86 pm). This substitution is possible because the Zr^{4+} is chemically more stable than the Ti^{4+} [4].

BZT presents good dielectric properties due to its low dielectric loss and reasonable dielectric constant [5–7]. The microwave dielectric properties of this material are interesting for the development of capacitive and nonvolatile memory cells (DRAM's and FeRAM's) [8–10]. Moreover, the dielectric properties and ferroelectric phase transition temperature (T_m) of BZT ceramics are strongly dependent of Zr content in the lattice. BZT bulk ceramics with Zr content up to $x > 0.08$ exhibit a broad dielectric constant-temperature ($\varepsilon \sim T$) curve near the T_m. This behavior can

L. S. Cavalcante (✉) · J. C. Sczancoski · M. T. Frabbro
LIEC,DQ-UFSCar, P.O. Box 676, 13565-905 Sao Carlos, SP, Brazil
e-mail: laeciosc@bol.com.br

J. C. Sczancoski
e-mail: jcsfisica@gmail.com

M. T. Frabbro
e-mail: tete_fabbro@hotmail.com

F. S. De Vicente · M. S. Li
Instituto de Física de São Carlos, USP, P.O. Box 369, 13560-970 Sao Carlos, SP, Brazil
e-mail: fsdevicente@nin.ufms.br

M. S. Li
e-mail: maximo@if.sc.usp.br

J. A. Varela · E. Longo
IQ, Universidade Estadual Paulista, P.O. Box 355, 14801-907 Araraquara, SP, Brazil
e-mail: varela@iq.unesp.br

E. Longo
e-mail: elson@iq.unesp.br

be caused by the inhomogeneous distribution of Zr^{4+} ions into the Ti sites and/or by the mechanical stresses on the grains [11]. When Zr content increases up to $x \sim 0.20$ is observed the limit between ferroelectric/relaxor behavior [4, 12]. Ravez and Simon [13] reported a typical relaxor-like behavior in BZT ceramics with Zr content up to $x \geq 0.25$. Tang et al. [14] showed that the BZT ceramics with a high Zr content ($x = 0.30$ and 0.35) present a "slim" hysteresis loop, which is a typical relaxor ferroelectric behavior due to the existence of micropolar regions. However, some studies on the optical properties of crystalline and non-crystalline BZT thin films have been reported in the literature, including: infrared optical properties [15, 16], complex refractive index [17–19] and photoluminescence [20–22].

The dielectric and ferroelectric properties of BZT thin films can be modified by different factors, mainly including: average grain sizes [23–25], preferred orientation [26–28], buffer layers [29, 30] and presence of dopants. Generally, BZT thin films have been doped with cerium [31, 32], neodymium [33], lanthanum [34] and manganese [35]. However, the literature reports few studies detailed on the surface microstructure and photoluminescence behavior of BZT thin films.

Therefore, we report on the microstructure, dielectric properties and optical band gap control on the photoluminescence behavior of $Ba[Zr_{0.25}Ti_{0.75}]O_3$ (BZT) thin films synthesized by the complex polymerization method and heat treated at 400 °C for different times and at 700 °C for 2 h.

2 Experimental details

2.1 Preparation of $Ba[Zr_{0.25}Ti_{0.75}]O_3$ thin films

BZT thin films were prepared by the complex polymerization method. In this synthesis, barium nitrate $Ba(NO_3)_2$ (99.9% purity, Aldrich), titanium (IV) isopropoxide $[Ti(OC_3H_7)_4]$ (99% purity, Aldrich), zirconium n-propoxide $[Zr(OC_3H_7)_4]$ (99.9% purity, NOAH Technologies), ethylene glycol ($C_2H_6O_2$) (99% purity, J.T. Baker) and citric acid ($C_6H_8O_7$) (99.5% purity, Mallinckrodt) were used as raw materials. Firstly, $[Ti(OC_3H_7)_4]$ was quickly added in citric acid aqueous solution to avoid hydrolysis reaction between alkoxide and air environment. Clear and homogeneous titanium citrate was formed under constant stirring at 90 °C for several hours. In the following step, the gravimetric procedure was realized for the correction and determination of the stoichiometric value correspondent to the TiO_2 mass (grams) contained into the titanium citrate. In the second stage, $[Zr(OC_3H_7)_4]$ was quickly added into the citric acid aqueous solution under constant stirring at 90 °C for several hours, forming a clear and homogeneous zirconium citrate. Again, the gravimetric procedure was employed to determine the ZrO_2 mass (grams) contained into the zirconium citrate. In the third stage, the titanium citrate and zirconium citrate were homogenized and mixed in a stoichiometric molar proportion of 0.75Ti:0.25 Zr. In the following step, $Ba(NO_3)_2$ was dissolved into the Ti, Zr citrates in a stoichiometric molar proportion of 1Ba:0.75Ti:0.25Zr. The solution pH was adjusted up to 7 by the addition of ammonium hydroxide (NH_4OH) (30% in NH_3, Synth). This procedure was employed to avoid barium citrate precipitation, which is favored in acid solutions. After solution homogenization containing Ba^{2+} cations, $C_2H_6O_2$ was added into the solution heated at 120 °C to promote the citrate polymerization by the polyesterification reaction [36]. In this system, the citric acid/ethylene glycol ratio was fixed at 60/40 wt%. After polyesterification reaction, the BZT polymeric resin was formed. In the sequence, this polymeric resin was filtered to avoid contamination by other impurity particles. The viscosity of this resin was adjusted up to 13 mPa s using a rheometer (Brookfield DV-III, USA). Afterwards, the polymeric resin was deposited on Pt(111)[150 nm]/Ti[50 nm]/SiO_2[400 nm]/Si(100) substrates through a spin coating (KW-4B, Chemat Technology, USA), operating at 7500 rpm for 20 s. After deposition, the thin films were placed on a hot plate at 150 °C for 10 min to remove the residual solvents. Finally, BZT thin films were heat treated at 400 °C for different times (1, 2, 4, 8 and 16 h) under oxygen flow and at 700 °C for 2 h under air atmosphere.

2.2 Characterizations of $Ba[Zr_{0.25}Ti_{0.75}]O_3$ thin films

BZT thin films were structurally characterized by X-ray diffraction (XRD) using a Rigaku-DMax 2500PC (Japan) with Cu-Kα radiation in the 2θ range from 20° to 60° with 0.02°/min. Fourier-transform infrared (FT-IR) spectroscopies were performed with a spectrometer Bruker-Equinox 55 (Germany) using a 30 ° specular reflectance accessory. The surface microstructure of BZT thin films were verified through an atomic force microscopy (AFM) (Digital Instruments, Nanoscope (R) IIIa, USA). High resolution field-emission gun scanning electron microscopy (FEG-SEM) (Supra 35-VP, Carl Zeiss, Germany) was employed to estimate the thickness of BZT films. The dielectric measurements were performed in a metal-thin film-metal configuration using a Hewlett-Packard (4194A) impedance/gain phase analyzer. The capacitance value was taken using a small AC signal of 10 mV at 100 kHz. The dielectric constant and dielectric loss were measured as a frequency function in the range from 100 to 10 MHz. These electrical properties were measured through Au electrodes of 3.1×10^{-4} cm^2 area deposited on the thin

film surface by the shadow mask evaporation method. In order to promote a contact with the platinum bottom electrode, a corner of the film was removed by a HF + HCl solution. Ultraviolet–visible (UV–vis) spectra were taken using a Cary 5G (Varian, USA) equipment. Photoluminescence (PL) measurements were performed using a Thermal Jarrel-Ash Monospec 27 monochromator and a Hamamatsu R446 photomultiplier. The 350.7 nm of a krypton ion laser (Coherent Innova, USA) was used as excitation source, keeping its output power at 200 mW. PL intensity was normalized by the thickness of BZT thin films. All measurements were performed at room temperature.

3 Results and discussion

3.1 X-ray diffraction analyses

Figure 1 shows the XRD patterns of BZT thin films heat treated at 400 °C for different times and at 700 °C for 2 h.

As it can be seen in Fig. 1, the increase of processing time and heat treatment temperature resulted in a structural organization of BZT thin films. BZT thin films heat treated at 400 °C for 1 and 2 h showed only the (100) plane due to the structural disorder degree. The (100) and (110) planes were verified in BZT thin films heat treated at 400 °C for 4 h, indicating an intermediary structural organization or presence of structural order–disorder. The thin films heat treated at 400 °C for 8 h and 16 h exhibit the (200) plane, which is characteristic of ordered structure. The highest degree of crystallization was observed for the BZT thin film heat treated at 700 °C for 2 h. This film presented a polycrystalline structure, containing the respective crystallographic planes: (100), (110), (200), (210) and (211). All diffraction peaks can be indexed to the cubic structure, in agreement with the respective "JCPDS" (Joint Committee on Powder Diffraction Standards) card No. 36-0019 [37]. In this work, BZT thin films deposited on Pt(111)/Ti/SiO_2/Si substrates exhibited a preferential orientation along the (110) direction, in agreement with the results obtained by Zhai et al. [38]. XRD patterns also showed that the Pt peak intensity increases with the heat treatment temperature and processing time. This behavior can be associated with the grain growth or recrystallization process of the Pt bottom electrode [39].

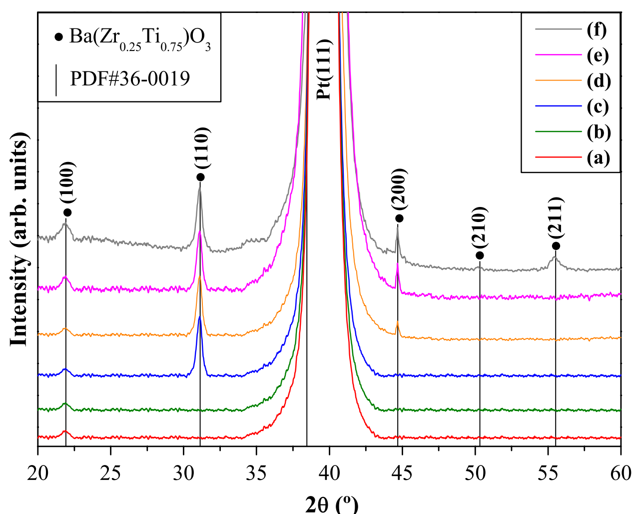

Fig. 1 XRD patterns of $Ba[Zr_{0.25}Ti_{0.75}]O_3$ thin films heat treated at 400 °C for: (a) 1 h, (b) 2 h, (c) 4 h, (d) 8 h, (e) 16 h under oxygen flow and at (f) 700 °C for 2 h under air atmosphere. The vertical lines indicate the position and relative intensity of JCPDS card No. 36-0019

3.2 Fourier-transform infrared analyses

Figure 2 shows the FT-IR spectra in the range from 550 cm^{-1} to 800 cm^{-1} of BZT thin films heat treated at 400 °C for different times and at 700 °C for 2 h.

In BZT thin films heat treated at 400 °C for 1 and 2 h were observed two absorption bands (Fig. 2a, b). The first band at 643 cm^{-1} was ascribed to the bond defects. We believe that the first band is formed by $[Zr,TiO_5]$ clusters

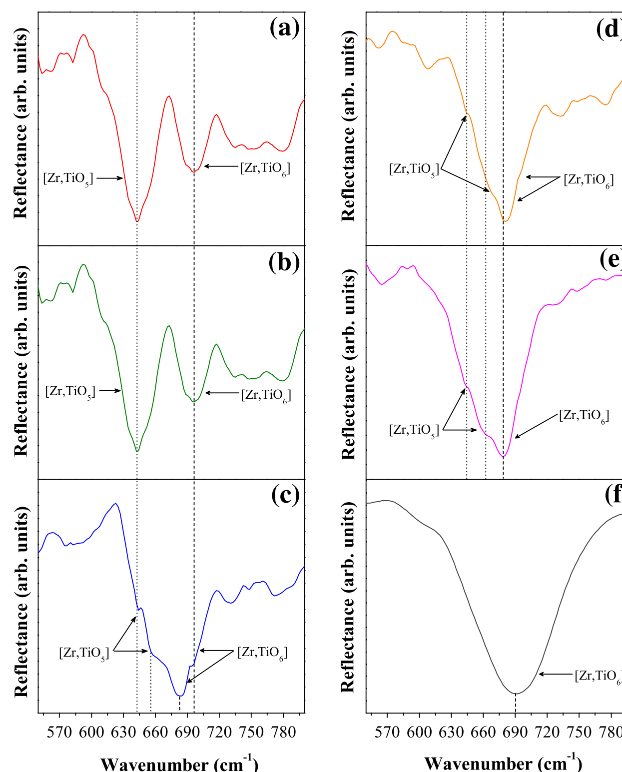

Fig. 2 FT-IR spectra of $Ba[Zr_{0.25}Ti_{0.75}]O_3$ thin films heat treated at 400 °C for: **a** 1 h, **b** 2 h, **c** 4 h, **d** 8 h, **e** 16 h under oxygen flow and at **f** 700 °C for 2 h under air atmosphere

with pyramidal-type configuration. This complex cluster was associated to the presence of oxygen vacancies ($V_O^{\bullet\bullet}$) between [O–Zr–O–Zr–$V_O^{\bullet\bullet}$] and/or [O–Ti–O–Ti–$V_O^{\bullet\bullet}$] bonds. The second band at 696 cm^{-1} was attributed to the metal–oxygen (M–O) band [40], suggesting the onset of formation of [Zr,TiO_6] clusters with octahedral-type configuration. The increase of processing time leads to a reduction of oxygen vacancies linked to the [Zr,TiO_5] clusters, favoring the structural organization of BZT thin films by the formation of [Zr,TiO_6]. In these figures, it was verified that the first band ([Zr,TiO_5] clusters) is relatively more intense than the second band ([Zr,TiO_6] clusters). Therefore, it is an indicative that the BZT thin films present a high degree of disorder in the lattice. When these thin films were heat treated at 400 °C for 4 h, it was observed the formation of a broad absorption band at 683 cm^{-1} caused by the junction between the two bands correspondent to the [Zr,TiO_5] and [Zr,TiO_6] clusters. The small band verified at 655 cm^{-1} is related to the [Zr,TiO_5] clusters (Fig. 2c). The increase of processing time promotes a displacement of this small band from 655 cm^{-1} to 662 cm^{-1}. Possibly, this behavior is associated with the reduction of oxygen vacancies ([Zr,TiO_5] clusters) in the BZT lattice (Fig. 2d, e). The increase of heat treatment temperature resulted in a broad absorption band at around 690 cm^{-1}, which was ascribed to the MO_6 stretching mode (M = Zr and Ti). In this case, MO_6 stretching modes are slightly shifted toward high wavenumbers and become sharper and narrower due to the resonance with the longitudinal optical (LO) phonon modes. This result suggests the formation of MO_6 octahedrons [41, 42] in the BZT lattice due to the increase of crystallinity and structural order of the BZT thin films [43].

3.3 Atomic force microscopy analyses

Figure 3 shows the AFM micrographs of BZT thin films heat treated at 400 °C for different times and at 700 °C for 2 h.

The surface microstrucuture was investigated by AFM over an area of 2.5 × 2.5 μm. BZT thin films heat treated at 400 °C for 1 h present a surface with uniform and homogeneous grain size distribution and low roughness (Fig. 3a). These results are in agreement with those reported by Choi et al. [44]. Figure 3b shows that the heat treatment of BZT thin films at 400 °C for 2 h leads to the grain growth. The increase of processing time for 4 h resulted in the formation of necks between grains, as shown in Fig. 3c. According to Leite et al. [45], this mechanism occurs by the grain boundary motion due to a reduction of the total grain boundary surface energy. The thermal energy leads to an increase in the diffusion rate and consequently intensifies the formation of necks between grains (Fig. 3d). As it can be seen in Fig. 3e, the increase of processing time for the BZT thin films under oxygen flow promotes an inhomogeneous growth on the surface. This inhomogeneous growth is caused by the formation of irregular grains and pore caused by the decomposition of residual organic compounds. This behavior is in agreement with the reported by Stankus et al. [46]. However, BZT thin films heat treated at 700 °C for 2 h under air atmosphere exhibited a homogenous and uniform microstructure formed by small grains (Inset of Fig. 3f). Moreover, small pore were verified on the surface of these films (arrows in Fig. 3f). This microstructural characteristic is similar for the BZT thin films prepared by the sol–gel method [47]. Thus, these results indicate that the atmosphere employed in the heat treatment is able to influence in the microstructure of thin films.

3.4 Field-emission gun scanning electron microscopy analyses

Figure 4 shows the FEG-SEM micrographs of surface microstructure and cross-section of BZT thin films heat treated at 400 °C for different times and at 700 °C for 2 h.

As it can be seen in this figure, the average thickness of BZT thin films heat treated at 400 °C from 1 h to 16 h under oxygen flow is reduced. Probably, this reduction is arising from the decomposition residual organic compounds and decreasing of oxygen vacancies [48]. The grain growth ocurrs by the reduction in the total grain boundary area and favors the junction between grains, resulting in the formation of necks (Inset in Fig. 4c) [49]. The heat treatment of BZT thin films at 400 °C for 8 h intensified the grain growth and contributed to the formation of pore (Inset and Fig. 4d). BZT thin film heat treated at 400 °C for 16 h exhibited the lowest average thickness (≈99 nm), reaching to the thickness limit of the film [50]. Also, it was observed the presence of large grains, which can be associated to the high crystallization rate of BZT thin films (Inset and Fig. 4e). The highest average thickness (≈145 nm) was verified for the thin films heat treated at 700 °C for 2 h under air atmosphere. Also, small grains and some pore were observed on the surface of these films. Therefore, it is an indicative that the atmosphere employed in the heat treatment results in modifications on the microstructural characteristic of BZT thin films (Inset and Fig. 4f).

3.5 Grain size, surface roughness and thickness analyses

Figure 5 shows the dependence of average grain size, average roughness and average thickness as a function of processing time for the BZT thin films.

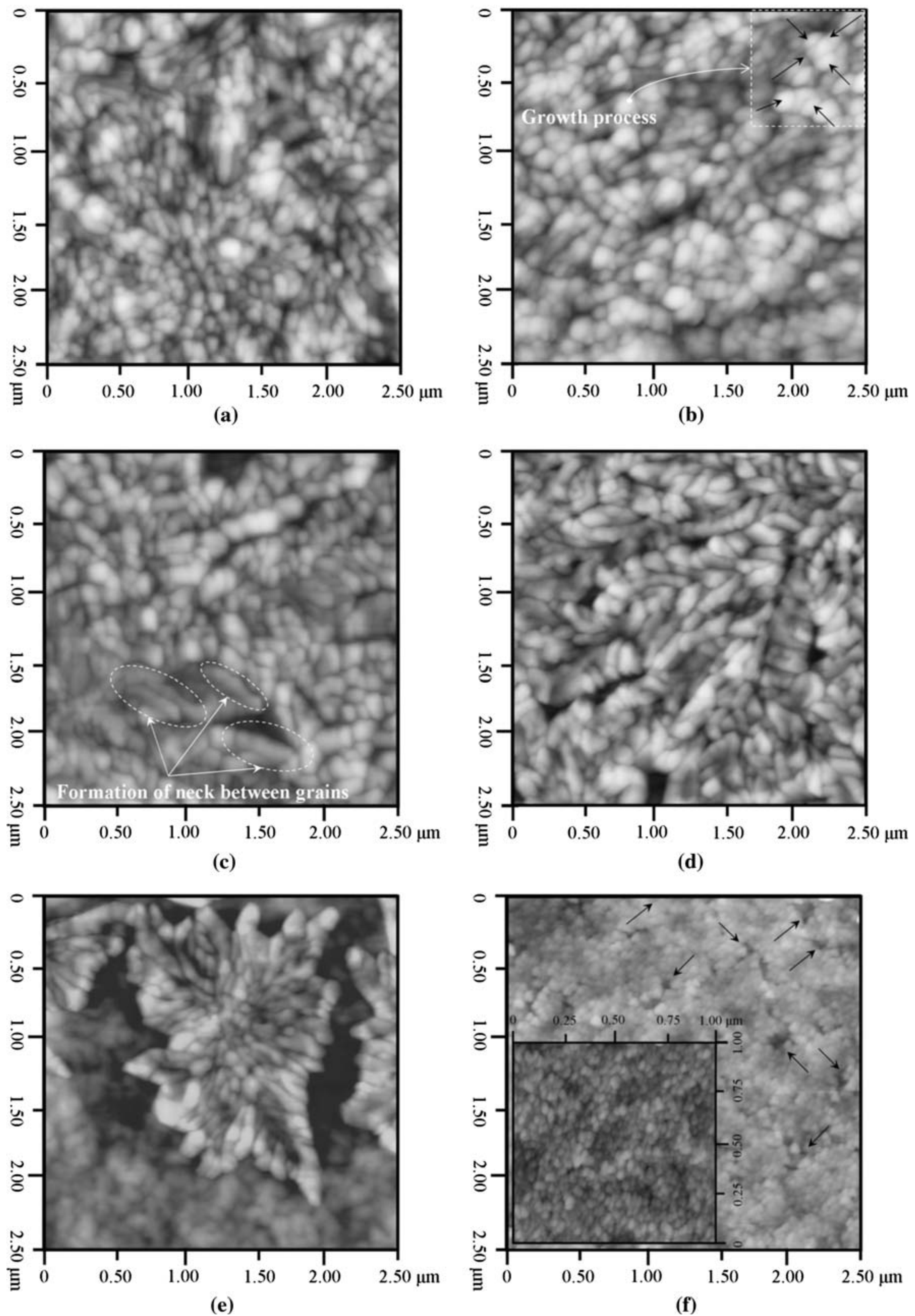

Fig. 3 AFM micrographs of $Ba[Zr_{0.25}Ti_{0.75}]O_3$ thin films deposited on $Pt(111)/Ti/SiO_2/Si(100)$ heat treated at 400 °C for: **a** 1 h, **b** 2 h, **c** 4 h, **d** 8 h, **e** 16 h under oxygen flow and at **f** 700 °C for 2 h under air atmosphere. Inset in **f** shows a high magnification AFM micrograph of the surface microstructure of BZT thin films heat treated at 700 °C for 2 h under air atmosphere

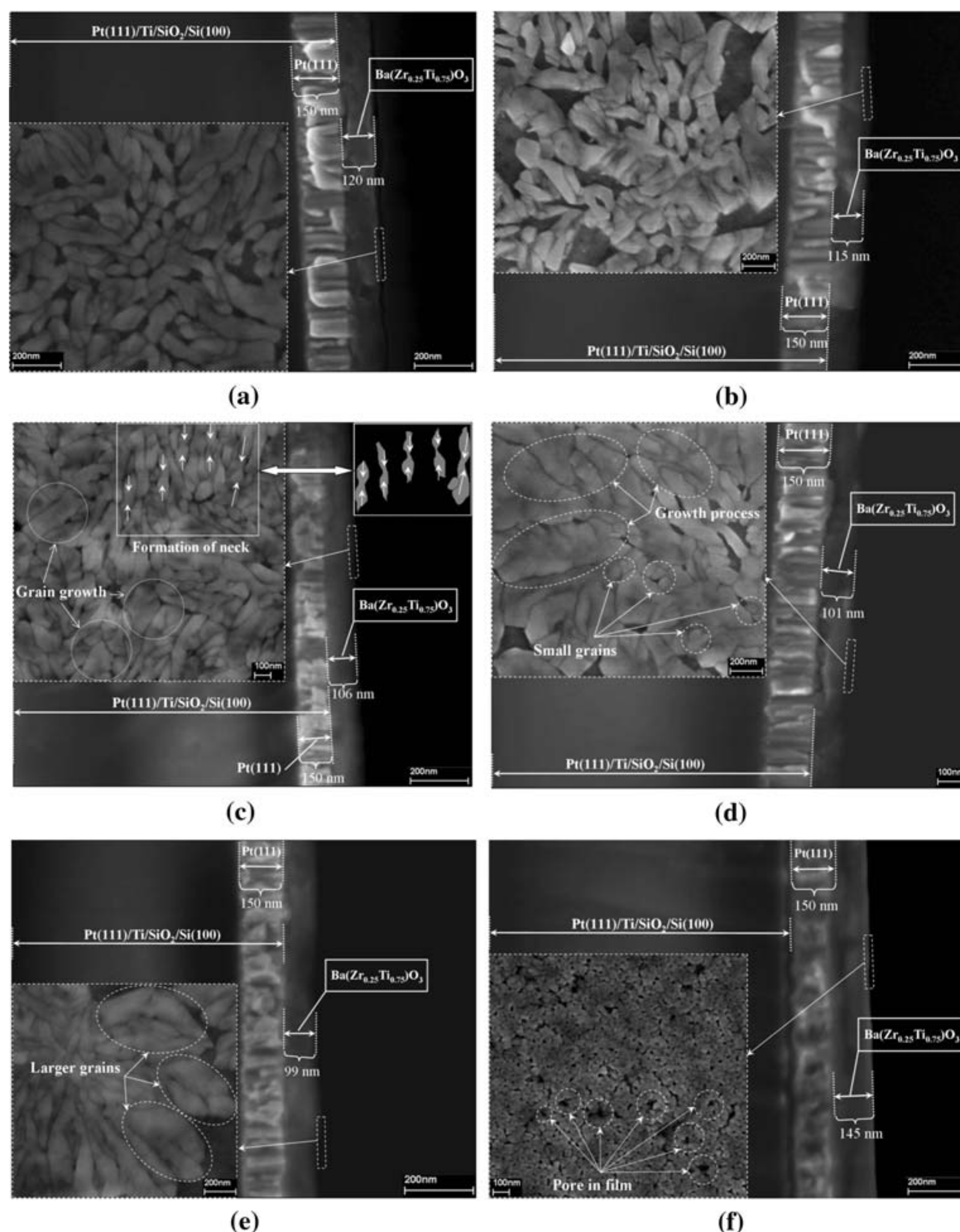

Fig. 4 FEG-SEM micrographs of the cross-section for $Ba[Zr_{0.25}Ti_{0.75}]O_3$ thin films deposited on Pt(111)/Ti/SiO_2/Si(100) and heat treated at 400 °C for: **a** 1 h, **b** 2 h, **c** 4 h, **d** 8 h, **e** 16 h under oxygen flow and at **f** 700 °C for 2 h under air atmosphere. Insets show the high magnification FEG-SEM micrographs of BZT thin films heat treated at 400 °C for different times under oxygen flow and at 700 °C for 2 h under air atmosphere

The average grain sizes and average surface roughness were calculated by the Nanoscope IIIa software-2003 (Version 5.12r5 for Windows XP professional) [51]. Thus, this program calculates the microstructural variables (average grain size and surface roughness) by the following equation:

$$R_{surf} = \sqrt{(\Sigma(Z_i)^2/N} \quad (1)$$

where R_{surf} is the average surface roughness, Z_i is the current Z (height) value and N is the number of sample points within the given area by the image.

Figure 5a shows a considerable variation in the average grain sizes with the processing time for the BZT thin films heat treated at 400 °C from 4 to 16 h. Probably, this behavior can be associated to the increase in the diffusion rate of grain boundaries with the processing time. In this case, this mechanism favors the formation of necks between grains, resulting in large grains. The increase in the average surface roughness of BZT thin films heat treated at 400 °C from 1 to 16 h can be relate to the formation of large grains, as previously described (Fig. 5a). The average thickness was estimated using the GNU Image Manipulation Program (GIMP 2.4) program [52]. As it can be seen in Fig. 5b, BZT thin films presented a reduction in the average thickness with the processing time. This result can be attributed to the decomposition of residual organic compounds. The obtained results by the AFM and FEG-

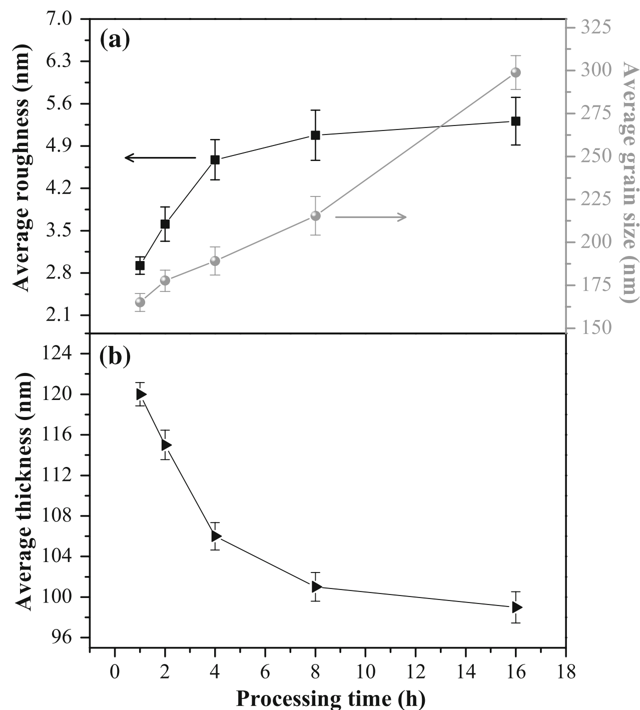

Fig. 5 The average grain size, average roughness and average thickness as a function of processing time of $Ba[Zr_{0.25}Ti_{0.75}]O_3$ thin films

SEM analyses for the BZT thin films are listed in Table 1. This table shows a comparative between average grain sizes, average roughness and average thickness of BZT thin films obtained in this work with those reported in the literature by different methods.

As it can be in this table, the average grain sizes, average roughness and average thickness are dependent of the preparation method, Zr content, heat treatment temperature and processing time. In this work, BZT thin films prepared by the CPM presented small deviations for the grain sizes (Fig. 5a), in agreement with the reported in the literature [53–56] (Table 1). We believe that the grain size control of BZT thin films prepared by the CPM and heat treated under oxygen flow is difficult and complicated because of the random grain growth with the processing time.

3.6 Dielectric properties

Figure 6 shows the frequency dependence of the dielectric constant (ε_r) and dielectric loss (tan δ) as a function of applied frequency of BZT thin films heat treated at 700 °C under air atmosphere.

In this figure, it was verified a slight decrease of the dielectric constant and a small increase of the dielectric loss with the frequency. Dielectric properties were not observed for the BZT thin films heat treated at 400 °C for different times, probably due to the presence of structural disorder in the lattice. The ε_r and tan δ of BZT thin film were 148 and 0.08 both at 1 MHz, respectively. The ε_r value is larger than the reported by Pantou et al. [57]. These authors synthesized $BaZr_{0.25}Ti_{0.75}O_3$ thin films by the metalorganic chemical vapor deposition and obtained a ε_r of approximately 130. Zhu et al. [58] reported a ε_r of 135 for the $BaZr_{0.2}Ti_{0.8}O_3$ films. They also showed that this electrical property increase up to 225 when doped with manganese. Recently, Xu et al. [59] observed a ε_r of 115 at 1 MHz for the nanocrystalline $BaZr_{0.2}Ti_{0.8}O_3$ thin films prepared by the sol–gel–ethanol thermal method. Qin et al. [60] showed that BST/BZT/BST multilayers films deposited on $LaNiO_3$-coated $LaAlO_3$ substrates exhibit a high ε_r ($\sim$414).

3.7 Ultraviolet–visible absorption spectroscopy analyses

Figure 7 shows the UV–vis absorbance spectra of BZT thin films heat treated at 400 °C for different times under oxygen flow and at 700°C for 2 h under air atmosphere.

The optical band gap energy (E_g) was estimated by the method proposed by Wood and Tauc [61]. According to these authors the optical band gap is associated with absorbance and photon energy by the following equation:

$$h\nu\alpha \propto (h\nu - E_g)^2 \qquad (2)$$

where α is the absorbance, h is the Planck constant, ν is the frequency and E_g is the optical band gap energy.

In this case, the E_g of BZT thin films were evaluated extrapolating the linear portion of the curve or tail. In Fig. 7, the small E_g values can be related to the presence of intermediary energy levels within the band gap of disordered BZT thin films. These energy levels are dependent of the degree of structural order–disorder in the lattice. Therefore, the increase of structural organization in the thin films leads to a reduction of these intermediary energy levels and consequently increases the E_g values (Fig. 7a–f). The E_g can be used to understand the PL behavior in the visible spectrum region. In this work, we attributed that the small E_g values are linked to the presence of deep holes and large concentration of defects. The deep holes are situated near from the valence band, which are related to the green–yellow–red emission components in the PL spectra at room temperature. The high E_g values of BZT thin films can be associated to the shallow holes and low concentration of defects. These intermediary energy levels are localized below the conduction band and act as blue emission components in the PL spectra at room temperature.

3.8 Photoluminescence behavior analyses

Figure 8 shows the PL spectra at room temperature of BZT thin films heat treated at 400 °C for different times under oxygen flow and at 700 °C for 2 h under air atmosphere.

Table 1 Average grain size, average roughness and average thickness of $Ba(Zr_xTi_{1-x})O_3$ thin films obtained in this work with those reported in the literature

Method	Zr content *x*	T (°C)	*t* (h)	Average grain size (nm)	Average roughness (nm)	Average thickness (nm)	Ref [ ]
CSD	0.20	700	–	30–50	1.4	50–150	[53]
PLD	0.20	650	0.166	40–50	8.5	400	[54]
SG	0.10	1100	2	100–120	–	600	[55]
R-FMS	0.20	400	1	–	0.845	150	[56]
R-FMS	0.20	500	1	5–150	1.655	150	[56]
R-FMS	0.20	600	1	100–300	6.614	150	[56]
CPM	0.25	400	1	165(±5.1842)	2.92(±0.143)	120(±1.154)	This work
CPM	0.25	400	2	177(±6.1584)	3.61(±0.283)	115(±1.451)	This work
CPM	0.25	400	4	189(±8.1454)	4.67(±0.332)	106(±1.348)	This work
CPM	0.25	400	8	215(±11.254)	5.07(±0.415)	101(±1.418)	This work
CPM	0.25	400	16	298(±9.8578)	5.31(±0.394)	99(±1.541)	This work
CPM	0.25	700	2	70(±4.2848)	3.05(±0.315)	145(±1.712)	This work

T Temperature, *t* Time, *Ref* Reference, *CSD* Chemical solution deposition, *PLD* Pulsed laser deposition, *SG* Sol-gel, *R-FMS* Radio-frequency magnetron sputtering, *CPM* Complex polymerization method, *Obs* All BZT thin films reported in the literature were deposited on platine substrates

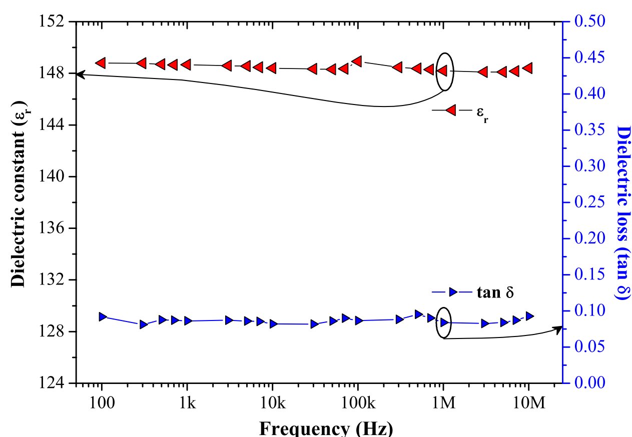

Fig. 6 Frequency dependence of the dielectric constant (ε_r) and dielectric loss (tan δ) as a function of applied frequency for BZT thin films heat treated at 700 °C for 2 h under air atmosphere

In Fig. 8, it was observed that the general aspect of the PL spectra is a broad band covering a large part of the visible electromagnetic spectrum, with a maximum emission situated at around 586 nm (yellow emission). PL profiles of BZT thin films suggest an emission mechanism by multiphonon or multilevel process, i.e., a system in which the relaxation occurs by means of different paths, involving the participation of several energy states within the band gap of the material. Therefore, in order to estimate the contribution of each individual component it was necessary to deconvolute the PL spectra. The deconvolution was performed trough the PeakFit program (4.05 version) [62] using the Pseudo Voigt function. The deconvolution results show that the PL profiles were better adjusted by the addition of five peaks (P_1—blue emission component, P_2 and P_3—green emission components, P_4—orange emission component, P_5—red emission component). Table 2 shows the contribution of each individual component on the PL spectra.

As it can be seen in Table 2, the increase of processing time leads to a reduction in the P_5 area or red emission component. This behavior can be linked to the reduction of structural disorder in the lattice of BZT thin films, in agreement with the XRD patterns (Fig. 1). In addition, BZT thin films heat treated at 400 °C from 1 to 4 h showed a considerable increase in the P_1 and P_2 areas, i.e., blue and green emission components, respectively. We believe that the changes on the P_1 and P_2 areas of BZT thin films heat treated at 400 °C for 4 and 8 h is caused by the transition from disordered to ordered structure. In Fig. 8f, it was observed an increase of the yellow PL emission of BZT thin films heat treated from 1 to 4 h due to the presence of structural order–disorder in the lattice. Therefore, these results indicate that the increase of heat treatment temperature and/or processing time favors the formation of ordered structures, reducing the PL emission of the material.

4 Model: optical band gap control on the photoluminescence behavior of BZT thin films

Figure 9 shows a proposed model to explain the PL behavior of BZT thin films through the optical band gap control.

Figure 9a shows the laser employed in the excitation of BZT thin films heat treated at 400 °C for different times

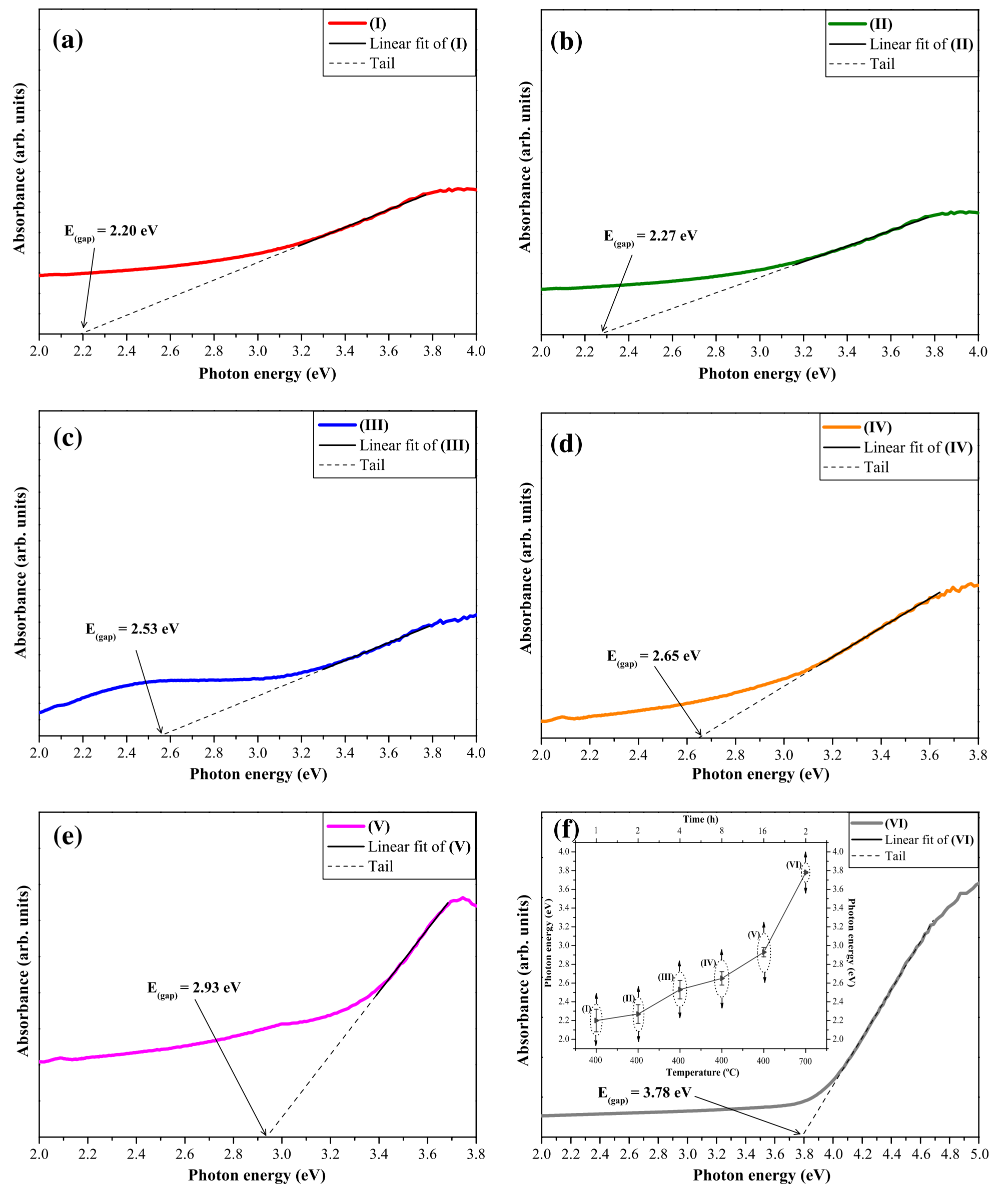

Fig. 7 UV–vis absorbance spectra of $Ba[Zr_{0.25}Ti_{0.75}]O_3$ thin films heat treated at 400 °C for: **a** 1 h (I), **b** 2 h (II), **c** 4 h (III), **d** 8 h (IV), **e** 16 h (V) under oxygen flow and heat treated at **f** 700 °C for 2 h (VI) under air atmosphere. Inset shows the optical band gap evolution as a function of processing time and heat treated temperature. The vertical bars show the standard mean error

under oxygen flow and at 700 °C for 2 h under air atmosphere. Figure 9b–f shows that the E_g values of BZT thin films heat treated at 400 °C from 1 to 8 h are associated with the presence of intermediary energy levels within the band gap. These energy levels are composed by oxygen 2*p* states (near from the valence band), zirconium 3*d* and titanium 4*d* states (below the conduction band). During the excitation process with 350.7 nm wavelength, some electrons are promoted from the oxygen 2*p* states to titanium 3*d* and/or zirconium 4*d* states by means of absorption of photons ($h\nu$) (gray arrows and Fig. 9b). The emission process of photons ($h\nu'$) occurs when the electrons localized on 3*d* or 4*d* states decays into an empty oxygen 2*p* states (gray arrows). Our results indicate that the visible light emission components (P_1, P_2, P_3, P_4 and P_5) associated to the PL emissions of BZT thin films are controlled by the optical band gap values [63]. Thus, each light emission in the visible electromagnetic spectrum can be linked to a respective band gap value (black arrows and electromagnetic spectrum in Fig. 9). Figure 9c shows that each visible light emission component is responsible for a kind of electronic transition from oxygen 2*p* states to titanium 3*d* and/or zirconium 4*d* states. Consequently, this mechanism is able to control the PL behavior of BZT thin films.

5 Conclusions

BZT thin films were synthesized by the complex polymerization method and heat treated at 400 °C for different times under oxygen flow and at 700 °C for 2 h

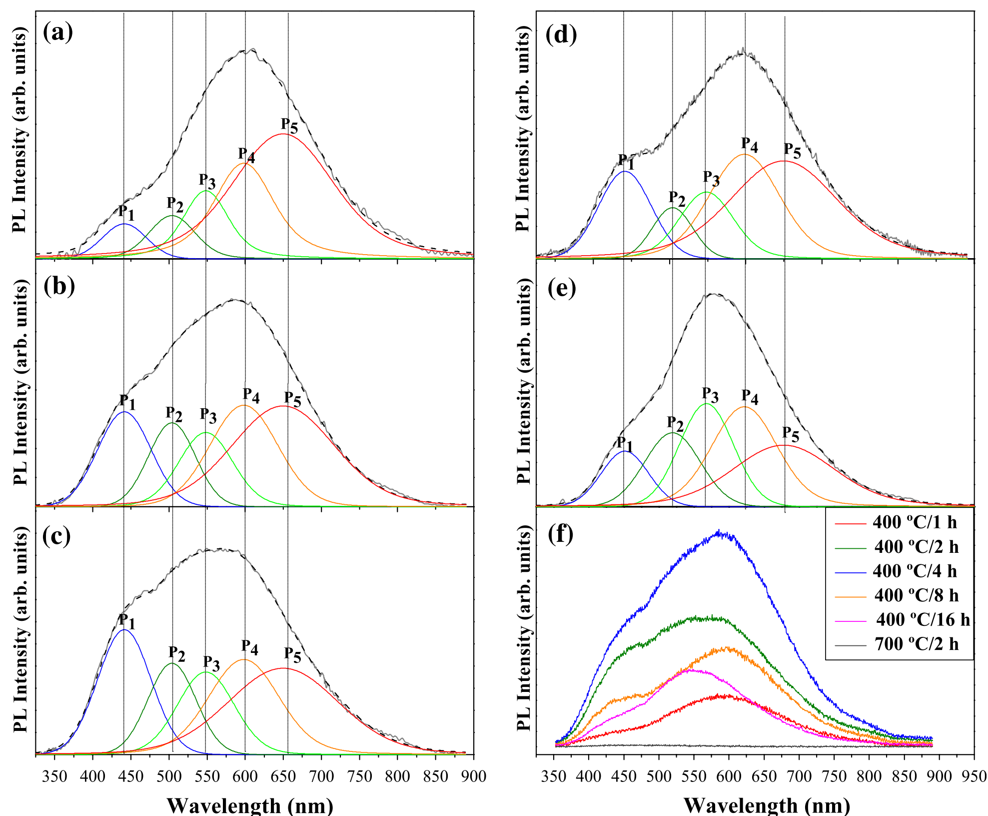

Fig. 8 PL spectra of $Ba[Zr_{0.25}Ti_{0.75}]O_3$ thin films heat treated at 400 °C for: **a** 1 h, **b** 2 h, **c** 4 h, **d** 8 h, **e** 16 h under oxygen flow. Deconvolution of each PL spectrum in five peaks with fixed position. **f** General PL spectra for $Ba[Zr_{0.25}Ti_{0.75}]O_3$ thin films heat treated at 400 °C for different times and heat treated at 700 °C for 2 h under air atmosphere

Table 2 Results obtained by the deconvolution of the PL spectra of BZT thin films heat treated at 400 °C for different times under oxygen flow

Annealing time (h)	Peak-P_1 center (nm)	Area of peak P1 (%)	Peak-P_2 center (nm)	Area of peak P_2 (%)	Peak-P_3 center (nm)	Area of peak P_3 (%)	Peak-P_4 center (nm)	Area of peak P_4 (%)	Peak-P_5 center (nm)	Area of peak P_5 (%)
1	441.455	5.16	503.912	7.25	548.375	12.67	598.24	24.42	649.852	50.50
2	441.455	16.02	503.912	12.48	548.375	13.27	598.24	22.62	649.852	35.61
4	441.455	19.91	503.912	13.13	548.375	14.54	598.24	21.76	649.852	30.66
8	441.455	15.00	503.912	6.72	548.375	12.78	598.24	25.98	649.852	39.52
16	441.455	9.89	503.912	15.53	548.375	21.08	598.24	26.92	649.852	26.58

P_1 Blue component, P_2 Green component, P_3 Green component, P_4 Orange component, and P_5 Red component

under air atmosphere. XRD patterns revealed that the thin films are free of secondary phases and crystallize in a cubic structure. FT-IR spectra suggested that the processing time leads to a increase of structural organization in the films through the transformation from $[Zr,TiO_5]$ to $[Zr,TiO_6]$ clusters. BZT thin films heat treated at 700 °C for 2 h exhibited a dielectric constant of approximately 148 at 1 MHz. AFM and FEG-SEM micrographs indicated that the BZT thin films present a homogeneous and smooth surface without the presence of cracks. These micrographs also showed that the grain growth can be associated with the increase in the diffusion rate of grain boundaries with the processing time. The reduction in the thickness was attributed to the decomposition of organic compounds and increase of crystallinity of the thin films. UV–vis absorption spectra showed that different optical band gap values are associated to the presence of intermediary energy levels within the band gap. In this case, it was verified that the increase of structural organization of BZT thin films with the processing time leads to a reduction of these energy levels and consequently increases the optical band gap. PL behavior of BZT thin films was explained through the optical band gap values associated to the control of different visible light emission components. The results also revealed that the blue emission component is due to the shallow holes while the green–yellow–red emission components are controlled by the deep holes within the band gap.

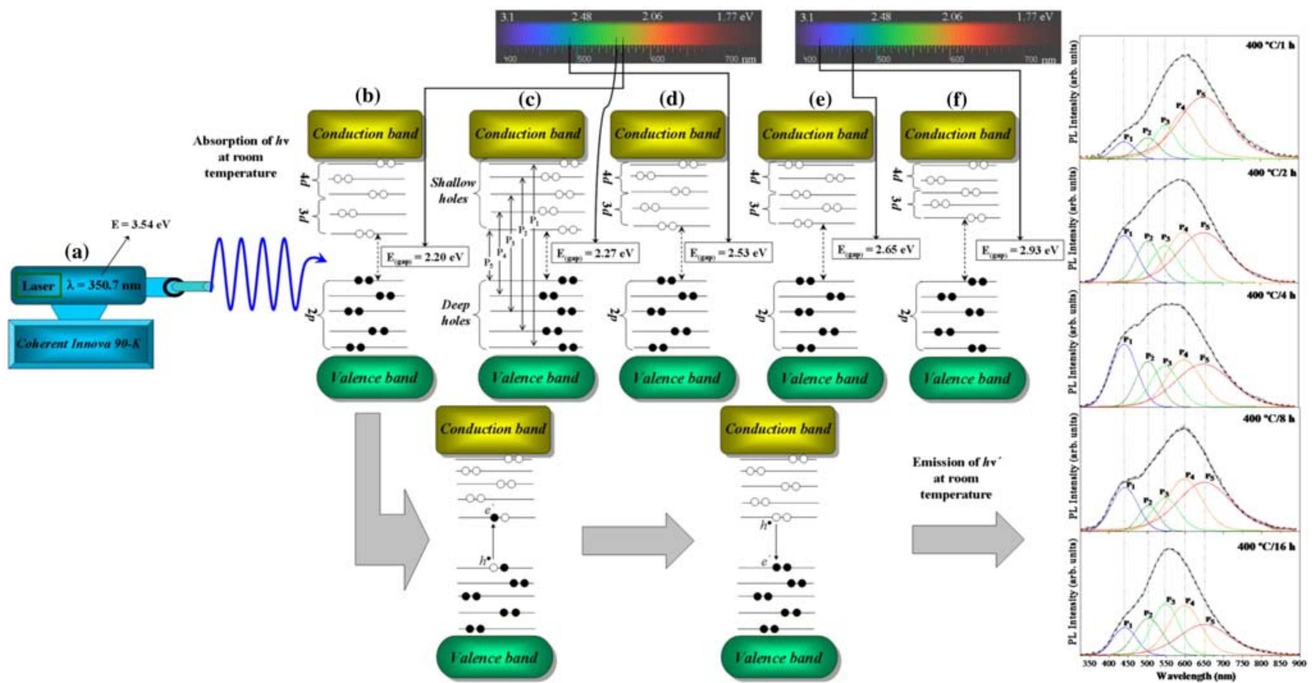

Fig. 9 Mechanism for the optical band gap control in photoluminescence behavior. (a) Laser employed in the excitation process of BZT thin films, (b) Wide Band Model, before excitation, Excitation—formation of self-trapped excitons (STE's), after excitation-recombination of e′ and $h^{\bullet}$ for the PL emission at room temperature. (c) Shallow and deep holes and peaks (P_1, P_2, P_3, P_4 and P_5) associated to the visible color centers. Wide Band Models for BZT thin film heat treated at 400 °C for (d) 4 h, (e) 8 h and (f) 16 h

Acknowledgments The authors thank the financial support of the Brazilian research financing institutions: CAPES, CNPq and FAPESP.

References

1. Yang C-F, Chen K-H, Chen Y-C, Chang T-C (2008) Appl Phys A 90:329
2. Dixit A, Agrawal DC, Mohapatra YN, Majumder SB, Katiyar RS (2007) Mater Lett 61:3685
3. Farhi R, El Marssi M, Simon A, Ravez J (1999) Eur Phys J B 9:599
4. Dixit A, Majumder SB, Savvinov A, Katiyar RS, Guo R, Bhalla AS (2002) Mater Lett 61:3685
5. Yun P, Wang DY, Ying Z, Zhou XY, Tian HY, Wang Y, Chan HLW (2007) Ferroelectrics 357:121
6. Marques LGA, Cavalcante LS, Simões AZ, Pontes FM, Santos-Júnior LS, Santos MRMC, Rosa ILV, Varela JA, Longo E (2007) Mater Chem Phys 105:293
7. Zhai J, Hu D, Yao X, Xu Z, Chen H (2006) J Eur Ceram Soc 26:1917
8. Zhu XH, Li J, Zheng DN (2007) Appl Phys Lett 90:142913
9. Wu TB, Wu CM, Chen ML (1996) Appl Phys Lett 69:2659
10. Xu J, Menesklou W, Ivers-Tiffée E (2004) J Electroceram 13:229
11. Weber U, Greuel G, Boettger U, Weber S, Hennings D, Waser R (2001) J Am Ceram Soc 84:759
12. Hennings D, Schnell A, Simon G (1982) J Am Ceram Soc 65:539
13. Ravez J, Simon A (1997) Eur J Solid State Inorg Chem 34:1199
14. Tang XG, Chew K-H, Chan HLW (2004) Act Mater 52:5177
15. Xu J, Gao C, Zhai J, Yao X, Xue J, Huang Z (2006) J Cryst Growth 291:130
16. Liu A, Xue J, Meng X, Sun J, Huang Z, Chu J (2008) Appl Surf Sci 254:5660
17. Tang XG, Chan HLW, Ding AL (2004) Thin Solid Films 460:227
18. Cheng WX, Ding AL, He XY, Zheng XS, Qiu PS (2006) J Electroceram 16:523
19. Xu J, Zhai J, Yao X (2007) Ferroelectrics 357:166
20. Anicete-Santos M, Cavalcante LS, Orhan E, Paris EC, Simões LGP, Joya MR, Rosa ILV, de Lucena PR, Santos MRMC, Santos-Júnior LS, Pizani PS, Leite ER, Varela JA, Longo E (2005) Chem Phys 316:260
21. Cavalcante LS, Gurgel MFC, Simões AZ, Longo E, Varela JA, Joya MR, Pizani PS (2007) Appl Phys Lett 90:011901
22. Cavalcante LS, Gurgel MFC, Paris EC, Simões AZ, Joya MR, Varela JA, Pizani PS, Longo E (2007) Acta Mater 55:6416
23. Zhai J, Yao X, Chen H (2004) Ceram Int 30:1237
24. Zhai J, Yao X, Shen J, Zhang L, Chen H (2004) J Phys D: Appl Phys 37:748
25. Pontes FM, Escote MT, Escudeiro CC, Leite ER, Longo E, Chiquito AJ, Pizani PS, Varela JA (2004) J Appl Phys 96:4386
26. Jiwei Z, Xi Y, Liangying Z, Bo S, Chen H (2004) J Cryst Growth 262:341
27. Zhang W, Tang XG, Wong KH, Chan HLW (2006) Scripta Mater 54:197
28. Miao J, Yuan J, Wu H, Yang SB, Xu B, Cao LX, Zhao BR (2007) Appl Phys Lett 90:022903
29. Gao LN, Song SN, Zhai JW, Yao X, Xu ZK (2008) J Cryst Growth 310:1245
30. Lan W-A, Wang T-C, Huang L-H, Wu T-B (2006) Appl Phys Lett 89:022910
31. Choi WS, Yi J, Hong B (2004) Mater Sci Eng B 109:146
32. Choi WS, Boo JH, Yi J, Hong B (2002) Mater Sci Semi Proc 5:211
33. Ostos C, Martínez-Sarrión ML, Mestres L, Cortés A, Delgado E, Prieto P (2006) Braz J Phys 36:1062
34. Gao L, Zhai J, Yao X (2008) Ceram Int 34:1023

35. Jie WJ, Zhu J, Qin WF, Wei XH, Xiong J, Zhang Y, Bhalla A, Li YR (2007) J Phys D: Appl Phys 40:2854
36. Kakihama M (1996) J Sol-Gel Sci Technol 6:7
37. http://www.icdd.com/profile/overview.htm
38. Zhai J, Gao C, Yao X, Xu Z, Chen H (2008) Ceram Int 34:905
39. Park Y, Jeong SM, Moon SIl, Jeong KW, Kim SH, Song JT, Yi J (1999) Jpn J Appl Phys 38:6801
40. Chakrabarti N, Maiti HS (1996) J Mater Chem 6:1169
41. Chen C, Zhu W, Yu T, Chen X, Yao X, Krishnan RG (2003) Surf Coat Technol 167:245
42. Last JT (1957) Phys Rev 105:1740
43. Cavalcante LS, Anicete-Santos M, Pontes FM, Souza IA, Santos LPS, Rosa ILV, Santos MRMC, Santos-Júnior LS, Leite ER, Longo E (2007) J Alloys Comp 437:269
44. Choi WS, Jang BS, Roh Y, Yi J, Hong B (2002) J Non-Cryst Solids 303:190
45. Leite ER, Varela JA, Longo E, Paskocimas CA (1995) Ceram Int 21:153
46. Stankus V, Dudonis J, Pranevicius L, Praneviius LL, Milcius D, Templier C, Riviere J-P (2003) Thin Solid Films 426:78
47. Jiwei Z, Xi Y, Bo S, Liangying Z, Chen H (2003) J Electroceram 11:157
48. Cavalcante LS, Anicete-Santos M, Sczancoski JC, Simões LGP, Santos MRMC, Varela JA, Pizani PS, Longo E (2008) J Phys Chem Solids 69:1782
49. Gouvêa D, Castro RHR (2003) App Surf Sci 217:194
50. Schintke S, Messerli S, Pivetta M, Patthey F, Libioulle L, Stengel M, De Vita A, Schneider W-D (2001) Phys Rev Lett 87:276801
51. http://www.thomaschi.com/dicom/di_index.html
52. http://www.gimp.org/
53. Sakamoto W, Mimura K-I, Naka T, Shimura T, Yogo T (2007) J Sol-Gel Sci Technol 42:213
54. Tang XG, Wang XX, Wong KH, Chan HLW (2005) Appl Phys A 81:1253
55. Dixit A, Majumder SB, Dobal PS, Katiyar RS, Bhalla AS (2004) Thin Solid Films 30:447
56 Choi WS, Jang BS, Lim D-G, Yi J, Hong B (2002) J Cryst Growth 237:438
57 Pantou R, Dubourdieu C, Weiss F, Kreisel J, Kobernik G, Haessler W (2003) Mater Sci Semicond Process 5:237
58 Zhu J, Jie WJ, Wei XH, Qin WF, Zhang Y, Li YR (2008) Surf Rev Lett 15:29
59. Xu J, Shen B, Gao L, Zhai J, Yao X (2008) Cryst Growth Des 8:1766
60. Qin WF, Zhu J, Xiong J, Tang JL, Jie WJ, Zhang Y, Li YR (2008) Surf Rev Lett 15:185
61. Wood DL, Tauc J (1972) Phys Rev B 5:3144
62. http://www.systat.com/products/PeakFit/
63. Luo L, Ren HZ, Tang XG, Ding CR, Wang HZ, Chen XM, Jia JK, Hu ZF (2008) J Appl Phys 104:043514